
Article:
Deng, Y. orcid.org/0000-0002-8804-9428, Xie, N., Hu, W. orcid.org/0000-0003-0254-8363 et al. (13 more authors) (2025) Disorder-induced electron localization and electronic states coupling in nitride semiconductors. Applied Physics Letters, 127 (25). 252101. ISSN: 0003-6951

https://doi.org/10.1063/5.0299514

Disorder induced electron localization and electronic states coupling in nitride semiconductors

Yong Deng[1†], Nan Xie[2†], Wenyu Hu[3†], Wenbin Qiu[4], Longqing Chen[5*], Yang Qiu[6*] Jian Ma[1], Xin Zhang[1], Yi Huang[1], Fujun Xu[7], Huiyun Liu[8], Xudong Cui[9], Xiaoyi Wang[1*], Pierre Ruterana[10], Veerendra C Angadi[11], Thomas Walther[11]

[1]Southwest Minzu University, State Ethnic Affairs Commission, Chengdu 610042, P. R. China

[2]Institute of Integrated Circuits, China Center for Information Industry Development, Beijing 100048, P. R. China

[3]Materials Characterization and Preparation Center and Department of Physics, Southern University of Science and Technology, Shenzhen 518056, P. R. China

[4]Department of Fundamental Courses, Wuxi Institute of Technology, WuXi 214121, P. R. China

[5]Key Laboratory of Radiation Physics and Technology of Ministry of Education, Institute of Nuclear Science and Technology, Sichuan University, Chengdu, 610064, P. R. China

[6]Pico Center, SUSTech Core Research Facilities, Southern University of Science and Technology, Shenzhen 518055, P. R. China

[7]State Key Laboratory of Artificial Microstructure and Mesoscopic Physics, School of Physics, Peking University, Beijing 100871, P. R. China

[8]Department of Electronic and Electrical Engineering, University College London, Torrington Place, London, WC1E 7JE, UK.

[9]School of Optoelectronic Science and Engineering, University of Electronic Science and Technology of China, Chengdu, 611731, P. R. China

[10]CIMAP, UMR 6252, CNRS-ENSICAEN-CEA-UCBN, 6 Boulevard Maréchal Juin, 14050 Caen Cedex 04, France

[11]School of Electrical & Electronic Engineering, University of Sheffield, Mappin St., Sheffield S1 3JD, U.K.

Abstract

The electronic states of surface oxidized nitride semiconductors (GaN, AlGaN and AlN) are investigated by valence electron energy-loss spectroscopy. It is shown that the loss of long-range atomic order in the surface oxide produces localized electronic states below the surface states in the bandgap. Using an off-axis electron probe, the coupling between local electronic states and localized states in the amorphous layers of GaN, AlGaN and AlN are studied. Regarding the excitation of surface states under aloof conditions via long-range electrostatic forces, the surface and the localized states are independent of electron scattering vector. Interestingly, though the surface sub-bandgap transitions are directionally forbidden, localized states show dispersion due to states coupling between bulk electronic states and localized states. These findings challenge the conventional model of built-in potential barriers at surface oxides and should be useful in understanding the local electrical properties of nano-scale structures.

Nitride semiconductors (GaN, AlN, InN) serve as cornerstone materials for high-efficiency light emitting devices (LEDs) and high-power electronic devices. However, their heteroepitaxial growth on conventional substrates inevitably introduces defects due to inherent material property disparities in lattice parameters, elastic constants, thermal expansion coefficients, and growth temperatures. These defects can persist even in strained heterostructures that form the active regions of most devices, encompassing both point defects[1,2] and extended defects such as threading dislocations[3,4], inversion domains[5,6], and stacking faults[4]. Of particular significance are defect-induced localized electronic states that interact with interband transitions[1,2,7], and can act as nonradiative recombination centers that compete with radiative electron-hole recombination—the fundamental process in light emission. This effect is clear in AlGaN-based UV-LEDs, where internal quantum efficiency drops from 46% to 34% when the threading dislocation density exceeds 6×10^{7} cm^{-3},[8] highlighting the critical impact of defects on device performance.

Surface oxidation in nitride semiconductors, typically initiates at moderate temperatures (~800°C) and may occur at lower thermal regimes[9]. This process introduces structural disorder through randomized atomic arrangements at defect cores and surfaces, significantly disrupting Bloch wavefunction periodicity. Consequently, vacancy- and disorder-induced localized states emerge[10–12], potentially triggering complex electronic transition dynamics near nitride semiconductor surfaces.

Conventional models explain carrier localization via heterostructure band alignment where wider-bandgap oxides (e.g., Al_2O_3, ~8.7 eV) form potential barriers with narrower-bandgap nitrides (e.g., AlN, ~6.2 eV), confining carriers through classical band bending[13–15]. Quantum mechanically, however, the Feynman path integral formalism[16,17] reveals quantum interference effects that double backscattering probability compared to classical predictions[18,19]. This quantum enhancement dramatically suppresses electron diffusion in disordered systems, manifesting as exponential tails in EELS profiles below the conduction band minimum[20–22]. Notably, even when Al_2O_3 maintains its larger bandgap relative to AlN, disorder-induced localization can create electronic states below the AlN conduction band edge.

For ultrathin (<2 nm) amorphous Al_2O_3/AlN interfaces, electron localization lengths may exceed oxide thicknesses, enabling short-range quantum interactions across interfaces. These coupled interfacial states exhibit effective dispersion from scattering amplitude convolution between localized states. Using off-axis VEELS, we have probed oxidized tubular defects in AlN, uncovering clear evidence of lattice-disorder-induced in-gap states in contrast to crystalline α-Al_2O_3/AlN heterostructures where downward band bending occurs[23–25]. Key findings of this study include: 1) Localized state dispersion can be tuned via short-range coupling between electronic states. 2) Co-probing reveals scattering-vector-independent hybridization when incident and surface wavevectors are parallel. 3) Orthogonal momentum configurations suppress surface transitions, enabling coupling between localized states and bulk AlN bands. This behavior is observed across III-nitrides (GaN, $Al_{0.15}Ga_{0.85}N$, $Al_{0.4}Ga_{0.6}N$), challenging classical surface-potential-barrier models[24,26]. Instead, our work establishes disorder-

mediated in-gap states as a dominant mechanism, necessitating revised carrier transport models for oxidized nitride systems through observed transitions between dispersive and flat bands via state hybridization.

The AlN thin film was grown on α-Al_2O_3(0001) substrates patterned with a 1 μm-period hexagonal hole array (≈500 nm deep) via 365 nm UV lithography. Epitaxial growth of was carried out at 1270°C in a 3×2" CCS Aixtron metal-organic chemical vapor deposition system using tri-methyl aluminum and NH_3 precursors, producing AlN epilayers 5 μm thick that serve as a suitable model for the formation of tubular defects within the AlN film which will oxidize on their inner surfaces.[22]. The details of AlN growth parameters can be found in our recent publication[23]. Specimens for transmission electron microscopy (TEM) were prepared using a Thermo-Fisher Helios 600i FIB system with a Ga^+ ion beam. Initial milling was performed at 30 kV (0.23-9.3 nA) to create lamellae, followed by final thinning at 2 kV (<15 pA). Surface oxides were removed using a Fischione Nanomill 1040 operated at 900 eV and 150 pA for final polishing. The VEELS experiments were carried out on an extreme field-emission gun (XFEG) Thermo-Fisher Titan Themis Cube G2 double aberration corrected transmission electron microscope operated at 60 kV. Hence, Cherenkov radiation can be eliminated because at 60 kV the electron velocity can be calculated as 1.29×10^8 m/s from the relativistic formula[24] and so remains below the speed of light in AlN which can be estimated to lie in the range of $1.35\text{-}1.41\times10^8$ m/s [25], depending on the value of the dielectric function chosen. The electron microscope is equipped with a Gatan Quantum ER965 EELS system and a monochromator that allows an energy resolution of ~150 meV. Dual EELS spectrum images were recorded in scanning TEM (STEM) mode using a nominal dispersion of 0.025 eV per channel. The convergence semi-angle for the incident electron beam was 3.23 mrad and the collection semi-angle 3.5 mrad for recording off-axis VEELS in beam tilt experiments, which allow sampling of the dispersion curve for particular momentum transfers. The sampling of the spectrum image in real space was set as 5 nm where the delocalization of inelastic scattering can

be neglected[24]. The set-up is similar to that used in Dwyer's[26] work, and the technique to accurately evaluate the band-edge onset is based on our previous research[27]. The fitting window for background subtraction was from 0.6 eV to 2.5 eV for bulk AlN and amorphous oxides layer, and the Fowler-Nordheim model[28] was used to describe the zero-loss tail.[29]

In disordered systems with negligible particle interactions (e.g., amorphous layers), localized states can be effectively characterized by the local density of states (LDOS). As derived in Eq. (1), the electron energy-loss spectroscopy (EELS) intensity $\boldsymbol{I}(\boldsymbol{q},\boldsymbol{E})$ for these states exhibits a specific $\boldsymbol{q}$-dependence:

$$I(\boldsymbol{q},E) \propto |M|^2 N_{al}(E) \tag{1}$$

However, when the localization length exceeds the amorphous layer thickness, localized electrons can diffuse beyond the layer boundary. This enables coupling between localized states and surface/bulk states, thereby modifying the EELS intensity. The resulting hybridized state intensity $\boldsymbol{I}(\boldsymbol{q},\boldsymbol{E})$ is given by Eq. (2):

$$I(\boldsymbol{q},E) \propto |M_{sb}(\boldsymbol{q}) + M|^2 \left(N_{al}(E) \otimes N_{sb}(E)\right) \tag{2}$$

In this context, $\boldsymbol{M}_{sb}$ denotes the transition matrix for surface/bulk states, while $\boldsymbol{N}_{sb}$ represents the joint density of states (JDOS) of these states. The term $\boldsymbol{N}_{al}(\boldsymbol{E}) \otimes \boldsymbol{N}_{sb}(\boldsymbol{E})$ represents the convolution between the local density of states (LDOS) of localized states and the JDOS of surface/bulk states.

When $\boldsymbol{M}_{sb}$ is selected as the transition matrix for surface states probed under aloof conditions, long-range electrostatic interactions render $\boldsymbol{M}_{sb}$ only weakly dependent on the electron scattering vector $\boldsymbol{q}$. Consequently, the combination $|M_{sb}(\boldsymbol{q}) + M|^2$ becomes effectively $\boldsymbol{q}$-independent, resulting in a dispersion-free $\boldsymbol{I}(\boldsymbol{q},\boldsymbol{E})$ profile across momentum space.

In contrast, if $\boldsymbol{M}_{sb}(\boldsymbol{q})$ is chosen as the transition matrix for a momentum-dependent bulk state, its $\boldsymbol{q}$-dependence becomes essential. This $\boldsymbol{q}$-dependence enables momentum-

dependent coupling between localized and bulk states, introducing dispersion into the EELS intensity profile.

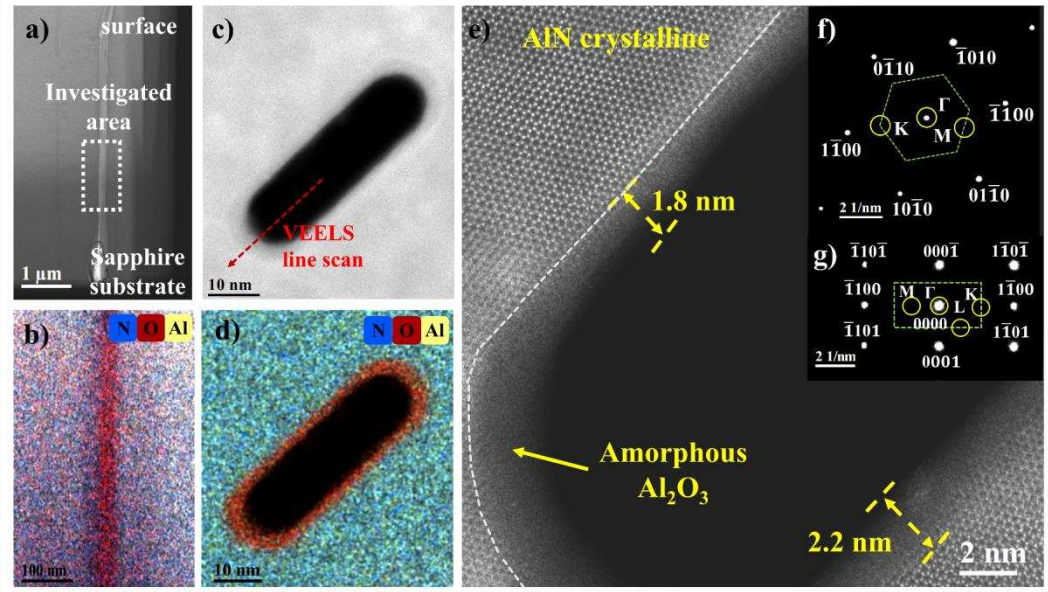

Figure 1. a) cross-sectional high-angle annular dark field (HAADF) image of a thin AlN film with a tubular defect in it. b) is an energy-dispersive X-ray spectrometry (EDXS) map from the area marked by the dotted white rectangle in a). c) is a top-down view onto such a cylindrical defect with an elliptical cross-section extracted from another plan-view sample, with corresponding EDXS map in d) and high-resolution HAADF image of the defect's edge in e). f) and g) show the diffraction patterns for specimen regions a) and c) and the corresponding aperture positions for VEELS experiments, respectively.

For systematic characterization of the band structure in surface-oxidized defects, precise evaluation of the oxide layer region and its crystallographic properties was imperative. Initial structural analysis was conducted through high-angle annular dark-field (HAADF) imaging of both plan-view and cross-sectional AlN specimens. Figure 1a reveals the tubular defect of ~80 nm widths extending toward the surface, while Figure 1c displays its plan view showing an elliptical geometry (~10×40 nm).

Subsequent elemental mapping (Figures 1b, d) confirmed ~2 nm surface oxidation within the defects, as evidenced by distinct oxygen signals (red).

High-resolution TEM imaging (Figure 1e) elucidated the atomic arrangement at the AlN/Al_2O_3 heterointerface. Well-defined lattice fringes in the AlN matrix reflect the epitaxial crystalline phase grown on sapphire substrates. Notably, the characteristic hexagonal lattice symmetry dissipates at defect peripheries, indicating an oxidation-induced crystalline-to-amorphous phase transition.

The disruption of long-range atomic order in oxidized surfaces modifies reciprocal space symmetry, consequently altering the ***E-k*** dispersion relation[30]. This prompted comprehensive VEELS investigations under both on-axis (***q***=0) and off-axis conditions[31] (Figure S1). For on-axis measurements along [0001] (plan-view) and [$10\bar{1}0$] (cross-section) zone axes, the joint density of states (JDOS) was modeled by direct transitions following $I \propto \sqrt{E - E_g}$.[32] Bandgap extraction involved dual fitting approaches: square root function with constant offset and linear fitting to $\boldsymbol{I}^2$, with optimal energy windows selected via $\boldsymbol{R}^2$ maximization (Figures S2a-d). Comparative analysis revealed consistent AlN bandgap (5.81-5.87 eV), though square root fitting demonstrated superior precision (root mean-squared error (RMSE) $\pm$0.03 eV vs. $\pm$ 0.13 eV).

Off-axis VEELS measurements at high-symmetry points (K, L, M; Figure S3) required modeling indirect transitions via $I \propto (E - E_g)^{1.5}$.[33] Experimental bandgaps (Table 1) agrees with ab initio calculations performed using the Vienna Ab-initio Simulation Program (VASP) package with the HSE06 exchange correlation functional which is known to lead to most accurate band gaps for nitride materials[34]. The theoretical band structures exhibited excellent agreement with VEELS-derived dispersion relations, validating the experimental methodology for both AlN and α-Al_2O_3 systems.

Table 1. Comparison of the direct and indirect bandgaps measured by VEELS and computed by first principles using VASP with HSE06 functional for Γ, K, L and M points in AlN and in α-Al_2O_3, respectively. The error bars presented here incorporate both the spectrometer dispersion calibration error and the fitting error.[32]

	Γ (eV)	K (eV)	L (eV)	M (eV)
AlN (VEELS)	5.86±0.18	6.70±0.32	6.95±0.45	6.86±0.21
AlN (HSE06)	5.85	6.63	7.46	6.94
α-Al_2O_3 (VEELS)	8.96±0.6	10.82±0.27	9.74±0.26	11.15±0.19
α-Al_2O_3 (HSE06)	8.99	12.56	12.79	12.74

Given the wider bandgap of α-Al_2O_3 (8.71 eV) compared to AlN (5.85 eV), VEELS analysis of band alignment at the AlN/α-Al_2O_3 was carried out first. The line scans across the interface reveal the band diagram presented in Figure 2b, as can be seen, there is a characteristic band bending consistent with established AlN/ α-Al_2O_3 heterostructure models[35]. While a calculation of the joint density of states (JDOS) confirms direct bandgap transitions for both materials, we observe an interfacial JDOS tail exhibiting a $I \propto (E - E_g)^{1.5}$energy dependence, which extends up to 5.57 eV (as marked in fig. 2c), indicative of indirect bandgap behavior.

High-resolution scanning transmission electron microscopy (HRSTEM) imaging (Figure 2a) verifies the epitaxial nature of the interface, with no amorphous interlayers. The observed ~0.3 eV energy dip in Figure 2b - representing the energy difference between the bulk AlN band edge (blue arrow, Figure 2c bottom spectrum) and the AlN/α-Al_2O_3 interface states (red arrow, Figure 2c middle spectrum) - likely stems from strong interfacial N-Al-O bond interactions[35], with the spatially resolved bandgap energy profile serving as a reference for surface-oxidized defect studies.

Complementary VEELS measurements across the AlN/vacuum interface (Figure 2d), were acquired where the aloof probe technique was employed to investigate AlN surface states via delocalization inelastic scattering. Notably, the ~2 nm amorphous

Al_2O_3 layer induces band transitions below surface state energies (Figure 2e), potentially facilitating electron trapping. Systematic exclusion of oxygen vacancies, carbon contamination, and Ga implantation effects is a prerequisite to being able to attribute this electron localization solely to amorphous phase disorder.

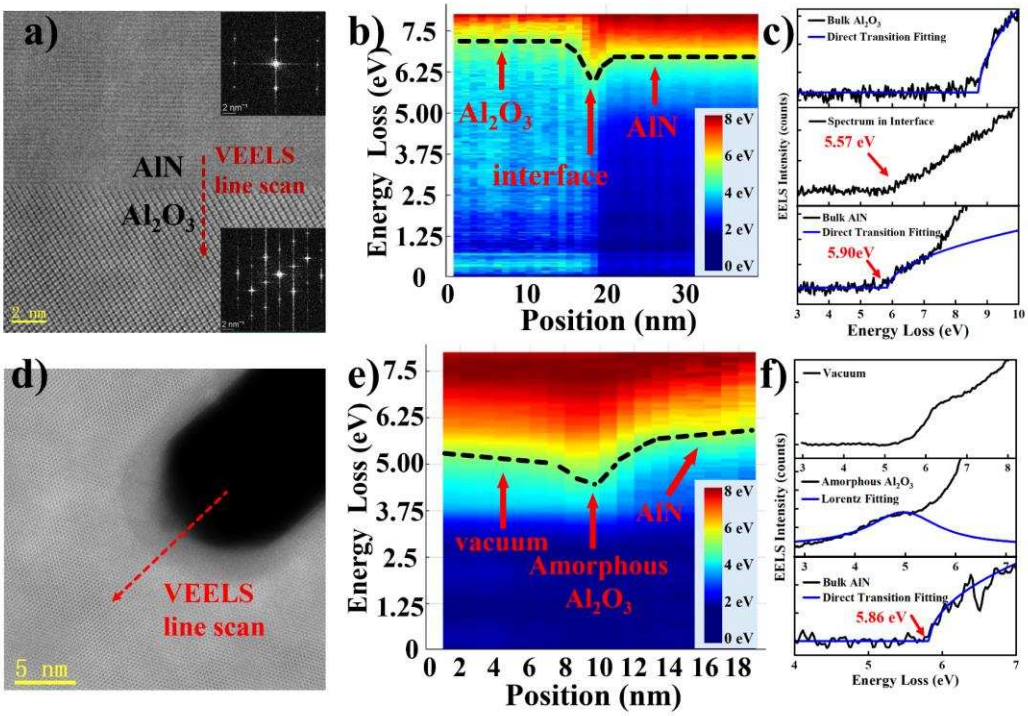

Figure 2. a) heterojunction of an AlN thin film on α-Al_2O_3 substrate across which VEELS has been conducted, b) shows the band diagram along the dotted red line in a). Spectra in c) correspond to bulk α-Al_2O_3, AlN and their interface as extracted from b). d) shows the heterojunction of AlN and surface amorphous α-Al_2O_3, across which further VEELS were recorded, with the resulting band diagram along the red line shown in e) and corresponding spectra in f).

To elucidate the energy level of oxygen vacancies in amorphous Al_2O_3, cross-sectional VEELS was employed to probe the band alignment between crystalline α-Al_2O_3 and its amorphous surface layer (Figure S4a). The spatial evolution of the low-energy loss features is presented in Figure S4b. While pronounced band bending is observed near the α-Al_2O_3 surface, the sub-bandgap transition onset energy at the α-Al_2O_3/amorphous-Al_2O_3 interface remains above 6.69 eV (Figure S4c). This indicates

that oxygen vacancies, despite their higher concentration in amorphous compared to crystalline Al_2O_3, cannot account for the joint JDOS tail observed below 5.9 eV (bandgap of AlN[36]) in surface-oxidized AlN.

For Ga-ion-implanted Al_2O_3 (Figure S4d), rather than exhibiting a JDOS tail at lower energies, the material demonstrates a bandgap reduction from 8.82 eV to 7.17 eV (Figure S4e-f), which still exceeds the bandgap/sub-bandgap transition energy of AlN. Furthermore, electron beam irradiation during STEM imaging may introduce localized carbon contamination on the specimen surface (Figure S4g), inducing additional band bending. However, the JDOS profile in carbon-contaminated regions reveals a broad dipole resonance centered at 6.05 eV[37], which again does not match the sub-bandgap JDOS features observed in amorphous alumina.

Since neither oxygen vacancies, Ga interstitials, nor carbon contamination can explain the ~5.6 eV transition observed in Figure 2e, we attribute this feature to the electronic structure of the disordered amorphous Al_2O_3 oxide layer.

For disorder-induced carrier localization phenomena, the characteristic localization tail observed in VEELS can be quantitatively described by a Lorentzian line profile[38], where the full width at half maximum (FWHM, denoted as $\hbar\omega$) serves as a direct metric for the degree of structural disorder. Crucially, the energy separation between the primary interband transition (E_b) and the localized states (E_c) follows the theoretical relationship as $E_c = \sqrt{E_b^2 - \hbar^2\omega^2}$.[39]

To experimentally verify the formation of amorphous Al_2O_3-induced localized states, we present the optical reflectance spectrum of an as-grown AlN sample in Figure S5. The spectrum exhibits a pronounced absorption onset at 210 nm (5.9 eV), exhibiting excellent agreement with the bandgap value of 5.85 eV determined by VEELS measurements. Through Tauc plot transformation of the reflectance data ($(\alpha hv)^2$ vs. photon energy E)[39,40], we observe remarkable consistency between the derived optical absorption profile and the squared VEELS intensity spectrum. Both techniques unambiguously reveal spectroscopic signatures of sub-bandgap states, manifested as a

Lorentzian-shaped feature centered at 4.5 eV with $\hbar\omega$= 1.5-2 eV. This multimodal analysis conclusively demonstrates that edge-oxidized alumina layers can introduce electronically active localized states within the forbidden bandgap of AlN.

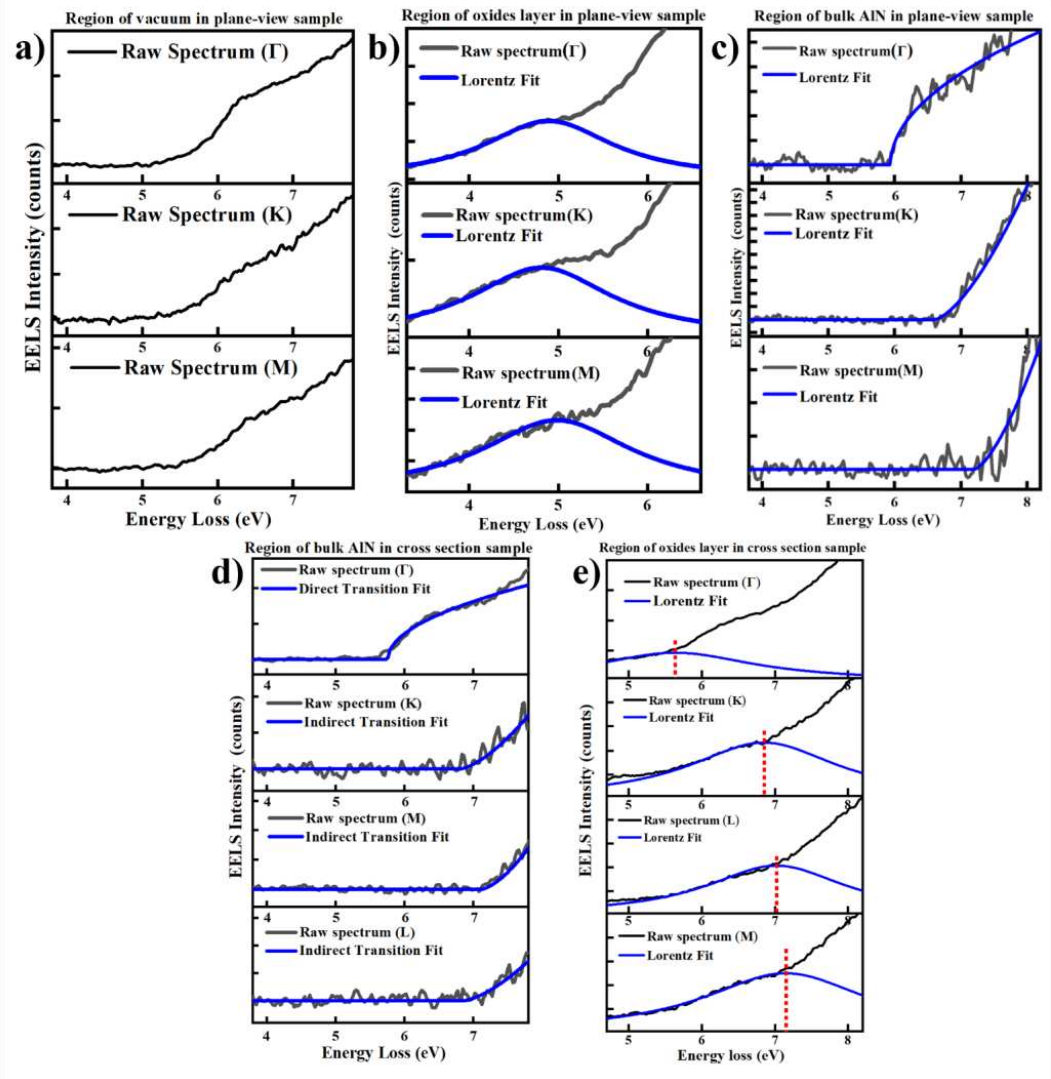

Figure 3. VEELS of a) edge-oxidized defect with aloof probe in plane-view, b) surface states from oxide in plane-view, c) bulk AlN in plane-view, d) bulk AlN in cross-section, e) the edge-oxidized defect in cross-section.

The oxidized tubular defect depicted in Figure 1(c)-(e) was systematically characterized using off-axis VEELS at high-symmetry points (Γ, K, M, and L) in the AlN Brillouin zone. This approach enabled spectral decomposition of bulk AlN, surface oxide layer,

and vacuum region components. Figure 3 presents the momentum-resolved contributions from these distinct states, where panels (a)-(c) demonstrate that while bulk AlN states exhibit expected dispersion, both surface states and localized states maintain constant energy positions regardless of the electron scattering vector $\boldsymbol{q}$. This anomalous behavior suggests strong hybridization between surface and localized states within the amorphous oxide matrix.

To verify this hypothesis, comparative on-axis and off-axis VEELS measurements were performed on thicker cross-sectional specimens (Figure S4). Under bright-field conditions with orthogonal alignment of incident electron beam and surface normal vectors, the surface state contribution became negligible. As evidenced in Figures 3(d)-(e), the resultant spectra revealed $\boldsymbol{q}$-dependent energy shifts not only for bulk AlN states but also for localized states, confirming bulk-localized state coupling. This phenomenon was consistently observed across various III-nitride systems including GaN, $Al_{0.4}Ga_{0.6}N$, and $Al_{0.15}Ga_{0.85}N$ (Figure S6), where the dispersion of localized states was similarly governed by their interaction with bulk/surface states. These findings imply that the electron localization length exceeds the thickness of ultrathin amorphous alumina layers, permitting wavefunction overlap between localized electrons and bulk AlN states.

Further investigation of beam-projection-dependent coupling effects was conducted through spatially resolved VEELS mapping. Figures 4 (plan-view) and Figure 5 (cross-sectional) present the reconstructed energy landscapes, featuring a characteristic ~2 eV FWHM broadening near defect edges. Through joint DOS analysis incorporating both direct and indirect transitions, we extracted the momentum-dependent interband transition energy $E_b(\boldsymbol{q})$. Notably, Figure 4 demonstrates that while bulk AlN exhibits conventional $E_b(\boldsymbol{q})$ dispersion, surface states under aloof-beam conditions maintain constant onset energies - conclusively eliminating any $\boldsymbol{q}$-dependence for states excited through long-range Coulomb interactions. The derived $E_c(\boldsymbol{q})$ maps (generated from $E_b(\boldsymbol{q})$ and FWHM distributions) further corroborate this interpretation, showing identical dispersion patterns to JDOS maps except within oxide regions where a $\boldsymbol{q}$-

independent localized state minimum appears. This provides definitive evidence for surface-localized state hybridization.

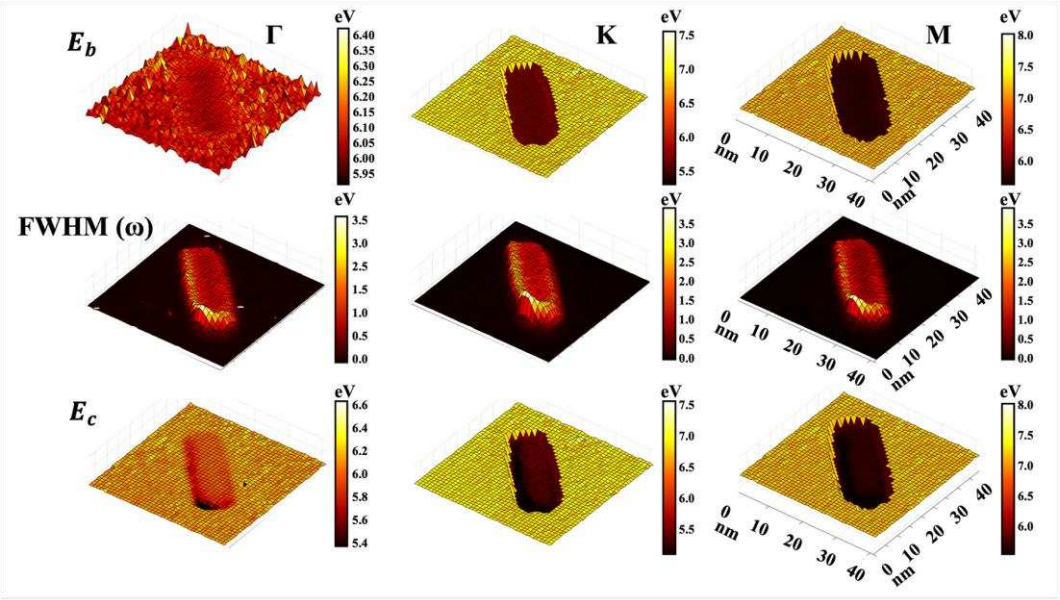

Figure 4. Localized state distribution based on VEELS. The ellipsoidal defect comes from the plan-view specimen. The fitted bandgap along various high symmetry directions is shown in the first row, the full width at half maximum (FWHM) after Lorentz function fitting is displayed as maps shown in the second row; the third-row plots localization energy (E_c) calculated from band-edge and ΔE maps. All scale bars are the same as for the last column.

To support this conclusion, VEELS of the defect core was recorded in cross-sectional view. By processing the energy landscape of E_b, FWHM and E_c in Figure 5, a broad FWHM of ~2.5 eV is observed only at the defect core, which confirms the presence of localized states. With the absence of surface sub-bandgap transitions, the localization energy (E_c) at the local defect shifts together with the change of band gap (E_b) from Γ to L points, which indicates a state coupling of bulk AlN band dispersion and localized states in surface oxides. Therefore, analyzing carrier localization in the surface oxide layer at the AlN defect requires an understanding of momentum-dependent inter-band transitions.

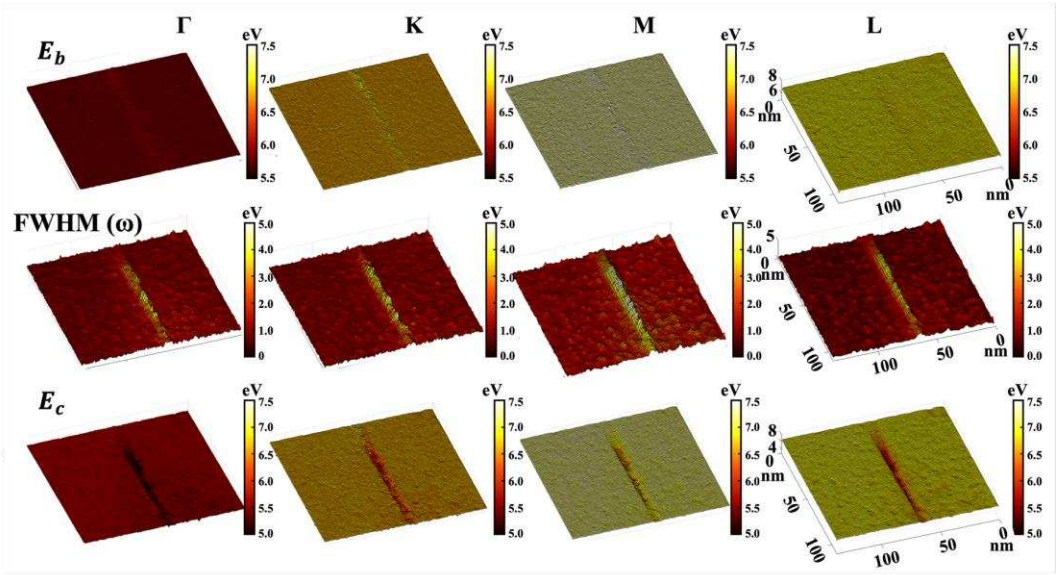

Figure 5. Maps of (top to bottom) bandgap E_b, FWHM ($\Delta E = \hbar\omega$), and localization energy E_c at different points extracted from the VEELS in cross-sectional view.

In summary, valence electron energy-loss spectroscopy (VEELS) reveals that the conventional α-Al_2O_3/AlN band alignment model fails to adequately describe electron dynamics at oxidized AlN surfaces. Through nanoscale off-axis VEELS mapping, we demonstrate that the band dispersion of localized states is governed by coupling between bulk electronic states and disorder-induced localized states. The plan-view geometry uniquely enables observation of state coupling between AlN surface states and localized states, where the surface states exhibit momentum independence a characteristic facilitating the formation of dispersion-free, disorder-induced localized states that effectively trap surface electrons. Remarkably, when probing the amorphous Al_2O_3/AlN interface in cross-section via electron beam irradiation, pronounced state coupling emerges between localized states and AlN bulk states. This interaction compels the localized states to develop distinct band dispersion, attributable to the convolution of scattering amplitudes between these coupled states. Notably, these phenomena are consistently observed in both GaN and AlGaN systems. Our findings underline the critical importance of probing disorder-induced localized states in dual spatial-momentum space for elucidating the impact of amorphous surface oxides on

electrical characteristics. Our newly identified mechanism provides fundamental insights into electronic behavior at amorphous/semiconductor interfaces, which play pivotal roles in determining the performance and reliability of diverse electronic devices.

The supplementary material provided shows the details of VEELS experiments and the determination of the bandgaps.

This work was supported by the Natural Science Foundation of the Jiangsu Higher Education Institutions of China (No. 24KJB490001) and also by the Fundamental Research Funds for the Central Universities， Southwest Minzu University (2020NYB39). The authors acknowledge the assistance of SUSTech Core Research Facilities for the aberration-corrected TEM experiments and acknowledge VC Angadi for provideing the code to analyze the bandgap, which can be downloaded on GitHub[41].

Author declarations

Conflict of interest

The authors have no conflicts of interest

Author information

Corresponding author

Xiaoyi Wang, Longqing Chen and Yang Qiu

Authors

Yong Deng; Xie Nan; Wenyu Hu; Wenbin Qiu; Jian Ma; Xin Zhang; Yi Huang; Fujun Xu; Xudong Cui; Pierre. Ruterana; Veerendra C Angadi; Thomas Walther

Author contributions

Yong Deng, Nan Xie and Wenyu Hu contributed equally to this paper

Yong Deng: Data curation (equal); Formal analysis (equal); Investigation (equal); Methodology (equal); Validation (equal); Visualization (equal); Writing– original draft (equal); Writing– review & editing (equal). **Nan Xie**: Formal analysis (equal); Writing– review & editing (equal). **Wenyu Hu**: Data curation (equal); Writing– review & editing (equal). **Wenbin Qiu**: Methodology (equal); Writing– review & editing (equal). **Longqing Chen**: Methodology (equal); Writing– review & editing (equal). **Yang Qiu**: Methodology (equal); Writing– review & editing (equal). **Jian Ma**: Investigation (equal); Writing–review & editing (equal). **Xin Zhang**: Investigation (equal); Writing– review & editing (equal). **Yi Huang**: Investigation (equal); Writing– review & editing (equal). **Fujun Xu**: Investigation (equal); Writing– review & editing (equal). **Huiyun Liu**: Investigation(equal); Methodology (equal). **Xudong Cui**: investigation (equal); Writing– review & editing (equal). **Xiaoyi Wang**: Conceptualization (equal); Funding acquisition (equal); Investigation (equal); Methodology (equal); Project administration (equal); Resources (equal); Supervision (equal); Writing– review & editing (equal). **Pierre Ruterana**: Supervision, Writing– review & editing (equal). **Veerendra C Angadi**: software, Writing–review & editing (equal). **Thomas Walther**: Supervision, Writing– review & editing (equal).

Data availability

The data that support the findings of this study are available from the corresponding author upon reasonable request.

REFERENCES

[1] D. Alden, J.S. Harris, Z. Bryan, J.N. Baker, P. Reddy, S. Mita, G. Callsen, A. Hoffmann, D.L. Irving, R. Collazo, and Z. Sitar, "Point-Defect Nature of the Ultraviolet Absorption Band in AlN," Phys. Rev. Appl. **9**(5), 054036 (2018).

[2] Y. Wu, D.A. Laleyan, Z. Deng, C. Ahn, A.F. Aiello, A. Pandey, X. Liu, P. Wang, K. Sun, E. Ahmadi, Y. Sun, M. Kira, P.K. Bhattacharya, E. Kioupakis, and Z. Mi, "Controlling Defect Formation of Nanoscale AlN: Toward Efficient Current

Conduction of Ultrawide-Bandgap Semiconductors," Adv. Electron. Mater. **6**(9), 2000337 (2020).

[3] V. Potin, P. Ruterana, G. Nouet, R.C. Pond, and H. Morkoç, "Mosaic growth of GaN on (0001) sapphire: A high-resolution electron microscopy and crystallographic study of threading dislocations from low-angle to high-angle grain boundaries," Phys. Rev. B **61**(8), 5587–5599 (2000).

[4] V. Potin, G. Nouet, and P. Ruterana, "Evidence for multiple atomic structure for the $\{10\bar{1}0\}$ inversion domain boundaries in GaN layers," Appl. Phys. Lett. **74**(7), 947–949 (1999).

[5] P. Vermaut, G. Nouet, and P. Ruterana, "Observation of two atomic configurations for the $\{1\bar{2}10\}$ stacking fault in wurtzite (Ga, Al) nitrides," Appl. Phys. Lett. **74**(5), 694–696 (1999).

[6] V. Potin, P. Ruterana, V. Potin, and G. Nouet, "HREM study of stacking faults in GaN layers grown over sapphire substrate," J. Phys.: Condens. Matter **12**(49), 10301 (2000).

[7] L. Jin, K. Zhao, S. Xu, Z. Qin, H. Cheng, L. Zhang, H. Qi, J. Li, R. Zheng, and H. Wu, "Optical property in colorless AlN bulk crystals: investigation of native defect-induced UV absorption," Scripta Mater. **190**, 91–96 (2021).

[8] H. Spende, C. Margenfeld, and A. Waag, "AlGaN Microfins as Nonpolar UV Emitters Probed by Time-Resolved Cathodoluminescence," ACS Photonics **9**(5), 1594–1604 (2022).

[9] K. Byczuk, W. Hofstetter, and D. Vollhardt, "Mott-Hubbard Transition versus Anderson Localization in Correlated Electron Systems with Disorder," Phys. Rev. Lett. **94**(5), 056404 (2005).

[10] W. Cheng, M. Zhao, Y. Lai, X. Wang, H. Liu, P. Xiao, G. Mo, B. Liu, and Y. Liu, "Recent advances in battery characterization using in situ XAFS, SAXS, XRD, and their combining techniques: From single scale to multiscale structure detection," (n.d.).

[11] Y. Xu, Q. Liu, J. Zhu, H. Zhang, J. Liu, R. Chen, J. Yu, Y. Li, and J. Wang, "Electron localization of ZnO/$ZnIn_2S_4$ interface induced lattice relaxation for triggering photocatalytic uranium evolution," Chem. Eng. J. **435**, 134958 (2022).

[12] R. Sawant, J. Samuel, A. Sinha, S. Sinha, and U. Sinha, "Nonclassical Paths in Quantum Interference Experiments," Phys. Rev. Lett. **113**(12), 120406 (2014).

[13] A.R. Barnea, O. Cheshnovsky, and U. Even, "Matter-wave diffraction approaching limits predicted by Feynman path integrals for multipath interference," Phys. Rev. A **97**(2), 023601 (2018).

[14] A.M.C. Souza, and H.J. Herrmann, "Flat-band localization in the Anderson-Falicov-Kimball model," Phys. Rev. B **79**(15), 153104 (2009).

[15] S.M. Girvin, and K. Yang, editors, "Anderson Localization," in *Modern Condensed Matter Physics*, (Cambridge University Press, Cambridge, 2019), pp. 252–300.

[16] Y. Luo, and A.J. Flewitt, "Understanding localized states in the band tails of amorphous semiconductors exemplified by α-Si:H from the perspective of excess delocalized charges," Phys. Rev. B **109**(10), 104203 (2024).

[17] K. Konstantinou, F.C. Mocanu, and J. Akola, "Electron localization in recrystallized models of the $Ge_2Sb_2Te_5$ phase-change memory material," Phys. Rev. B **106**(18), 184103 (2022).

[18] R. Atta-Fynn, P. Biswas, P. Ordejón, and D.A. Drabold, "Systematic study of electron localization in an amorphous semiconductor," Phys. Rev. B **69**(8), 085207 (2004).

[19] J.-J. Zhu, X.-H. Ma, W.-W. Chen, B. Hou, Y. Xie, and Y. Hao, "Comparative study on interface and bulk charges in AlGaN/GaN metal–insulator–semiconductor heterostructures with Al_2O_3, AlN, and Al_2O_3/AlN laminated dielectrics," Jpn. J. Appl. Phys. **55**(5S), 05FH01 (2015).

[20] C. Fares, F. Ren, M.J. Tadjer, J. Woodward, M.A. Mastro, B.N. Feigelson, C.R. Eddy, and S.J. Pearton, "Band offset determination for amorphous Al_2O_3 deposited on bulk AlN and atomic-layer epitaxial AlN on sapphire," Applied Physics Letters **117**(18), 182103 (2020).

[21] S. Ganguly, J. Verma, G. Li, T. Zimmermann, H. Xing, and D. Jena, "Presence and origin of interface charges at atomic-layer deposited Al_2O_3/III-nitride heterojunctions," Appl. Phys. Lett. **99**(19), (2011).

[22] Y. Li, C. Zhang, X. Luo, Y. Liang, D.-S. Wuu, C.-C. Tin, X. Lu, K. He, L. Wan, and Z.C. Feng, "Surface, structural and optical properties of AlN thin films grown on different face sapphire substrates by metalorganic chemical vapor deposition," Appl. Surf. Sci. **458**, 972–977 (2018).

[23] Y. Deng, N. Xie, W. Hu, Z. Ma, F. Xu, L. Chen, W. Qiu, L. Zhao, H. Tao, B. Wu, Y. Huang, J. Ma, X. Wang, X. Zhang, Y. Qiu, X. Cui, C. Jin, M.-P. Chauvat, P. Ruterana, and T. Walther, "Atomic Plane Misorientation Assisted Crystalline Quality Improvement in Epitaxial Growth of AlN on a Nanopatterned Sapphire (0001) Surface for Deep Ultraviolet Photoelectric Devices," ACS Appl. Nano Mater. **6**(6), 4262–4270 (2023).

[24] R.F. Egerton, "Electron Energy-Loss Spectroscopy in the Electron Microscope," Electron Energy-Loss Spectroscopy in the Electron Microscope, (2011).

[25] L. Gu, V. Srot, W. Sigle, C. Koch, P. van Aken, F. Scholz, S.B. Thapa, C. Kirchner, M. Jetter, and M. Rühle, "Band-gap measurements of direct and indirect semiconductors using monochromated electrons," Phys. Rev. B **75**(19), 195214 (2007).

[26] C. Dwyer, T. Aoki, P. Rez, S.L.Y. Chang, T.C. Lovejoy, and O.L. Krivanek, "Electron-Beam Mapping of Vibrational Modes with Nanometer Spatial Resolution," Physical Review Letters **117**(25), 256101 (2016).

[27] T. Walther, X. Wang, V.C. Angadi, P. Ruterana, P. Longo, and T. Aoki, "Study of phase separation in an InGaN alloy by electron energy loss spectroscopy in an aberration corrected monochromated scanning transmission electron microscope," Journal of Materials Research **32**(5), 983–995 (2017).

[28] H. Zhang, Y. Jimbo, A. Niwata, A. Ikeda, A. Yasuhara, C. Ovidiu, K. Kimoto, T. Kasaya, H.T. Miyazaki, N. Tsujii, H. Wang, Y. Yamauchi, D. Fujita, S. Kitamura, and H. Manabe, "High-endurance micro-engineered LaB_6 nanowire electron source for high-resolution electron microscopy," Nat. Nanotechnol. **17**(1), 21–26 (2022).

[29] T. Walther, E. Quandt, H. Stegmann, A. Thesen, and G. Benner, "First experimental test of a new monochromated and aberration-corrected 200kV field-emission scanning transmission electron microscope," Ultramicroscopy **106**(11), 963–969 (2006).

[30] V.M. Pereira, J.M.B. Lopes dos Santos, and A.H. Castro Neto, "Modeling disorder in graphene," Phys. Rev. B **77**(11), 115109 (2008).

[31] F.S. Hage, D.M. Kepaptsoglou, Q.M. Ramasse, and L.J. Allen, "Phonon Spectroscopy at Atomic Resolution," Phys. Rev. Lett. **122**(1), 016103 (2019).

[32] H. Amari, H.Y. Zhang, L. Geelhaar, C. Chèze, M.J. Kappers, and T. Walther, "Nanoscale EELS analysis of elemental distribution and band-gap properties in AlGaN epitaxial layers," J. Phys.: Conf. Ser. **326**(1), 012039 (2011).

[33] B. Rafferty, and L.M. Brown, "Direct and indirect transitions in the region of the band gap using electron-energy-loss spectroscopy," Phys. Rev. B **58**(16), 10326–10337 (1998).

[34] J. Heyd, G.E. Scuseria, and M. Ernzerhof, "Hybrid functionals based on a screened Coulomb potential," J. Chem. Phys. **118**(18), 8207–8215 (2003).

[35] X. Yan, Y. Jiang, Q. Jin, T. Yao, W. Wang, A. Tao, C. Gao, X. Li, C. Chen, H. Ye, and X.-L. Ma, "Interfacial interaction and intense interfacial ultraviolet light emission at an incoherent interface," Nat. Commun. **14**(1), 2788 (2023).

[36] V.O. Özçelik, J.G. Azadani, C. Yang, S.J. Koester, and T. Low, "Band alignment of two-dimensional semiconductors for designing heterostructures with momentum space matching," Phys. Rev. B **94**(3), 035125 (2016).

[37] S. Urbonaite, S. Wachtmeister, C. Mirguet, E. Coronel, W.Y. Zou, S. Csillag, and G. Svensson, "EELS studies of carbide derived carbons," Carbon **45**(10), 2047–2053 (2007).

[38] F. Höfling, T. Franosch, and E. Frey, "Localization Transition of the Three-Dimensional Lorentz Model and Continuum Percolation," Phys. Rev. Lett. **96**(16), 165901 (2006).

[39] J. Klein, L. Kampermann, B. Mockenhaupt, M. Behrens, J. Strunk, and G. Bacher, "Limitations of the Tauc Plot Method," Adv. Funct. Mater. **33**(47), 2304523 (2023).

[40] L. Samet, J. Ben Nasseur, R. Chtourou, K. March, and O. Stephan, "Heat treatment effect on the physical properties of cobalt doped TiO_2 sol–gel materials," Mater. Charact. **85**, 1–12 (2013).

[41] V.C. Angadi, C. Abhayaratne, and T. Walther, “Automated background subtraction technique for electron energy-loss spectroscopy and application to semiconductor heterostructures,” J. Microsc. **262**(2), 157–166 (2016).